Runout mechanism of landslides in alluvial basins with emphasis on the impact and erosion effects

Ye Chen[1,2], Fawu Wang[1,3], Maximillian Van Wyk de Vries[2], Weichao Liu[1], Bo Zhang[1], and Changbao Guo[4]

[1]Department of Geotechnical Engineering, Tongji University, Shanghai, China
[2]Cambridge Complex and Multihazard Research Group, Department of Earth Sciences & Geography, University of Cambridge, Cambridge, UK
[3]Key Laboratory of Geotechnical and Underground Engineering of the Ministry of Education, Tongji University, Shanghai, China
[4]Institute of Geomechanics, Chinese Academy of Geological Sciences, Beijing, China

Correspondence: Fawu Wang (wangfw@tongji.edu.cn)

Abstract. Landslide runout is a critical factor in risk assessment, and runout distance is the most widely used indicator of mobility. Runout distance is determined both by the landslide's initial conditions and through interactions with erodible substrates, which can affect momentum and inertia by altering basal friction and by increasing overall flow volume, generally increasing runout distance. During erosion, the landslide mass can exert sudden impact forces on the substrate at points where the slope changes abruptly. While erosion effects have been extensively discussed in prior studies, impact forces themselves have been overlooked. Here, we combine fieldwork in SE Tibet, laboratory tests, and numerical modelling to resolve the dynamics and effect of impact loading on landslides in alluvial basins. Impact-loading ring-shear tests and numerical simulations, backed up by field evidence, indicate that impact forces can near-instantaneously generate high excess pore water pressure within a saturated substrate, reducing basal friction of the landslide mass and extending runout. As density and geometry of the impactor determine a landslide impact force, both the impactor and substrate properties, including stiffness and compressibility, control the impact duration. The interplay of these two factors can lead to different landslide runout patterns and mobilities. The findings indicate that the farthest runout does not necessarily occur under the highest impact force; rather, an appropriate impact level exists that most effectively liquefies the substrate. The findings highlight the importance of considering substrate properties for both impact and erosion during landslide runout analyses, particularly those occurring in alluvial basins.

1 Introduction

Landslide is one of the most frequent and dangerous natural hazards in mountainous areas. A number of landslides travel unusually long runout distances, characterised by a very low apparent friction coefficient H/L (where H denotes the drop height and L the travel distance), which cannot be explained by simple friction models (Legros, 2002). These landslides have been observed across a wide range of environments, including subaerial, submarine, and even extraterrestrial settings such as the Moon (Goren and Aharonov, 2007). The mechanisms of long runout for such landslides vary from case to case, making it challenging to forecast or mitigate associated disasters.

Alluvial basins are widely distributed in mountainous regions. Due to their favourable topography, they often host dense populations and critical infrastructure. As depositional sites for converging water and sediment, alluvial basin floors typically feature gentle slopes and contain loose, highly saturated sediments. They are particularly susceptible to dynamic interactions with incoming landslide materials. It is well established that interaction between the landslide mass and materials along its path - through known as erosion or entrainment (Mangeney, 2011; Crosta et al., 2015; Pudasaini, 2025) - affects the mobility of the landslide by altering the volume and velocity of the landslide (Pudasaini and Fischer, 2020). Under specific conditions, this interaction can reduce basal friction, reducing energy losses and enabling the landslide to travel exceptionally long distances. It can be commonly observed that the runout of a landslide is extended by these material interactions, especially when water is involved at the same time. Examples include the well-studied 1903 Frank Slide from the east face of Turtle Mountain in Canada (Cruden and Hungr, 1986) (Fig. 1a). The detached rock covered almost 2 km of the Crowsnest River floodplain. Although evidence showed that the erosion volume was limited, it is believed that high pore water pressure was generated along the path where the landslide overrode loose and saturated soils (Hungr, 2017). Similarly, there was a disastrous rockslide-debris avalanche in February 2006 on Leyte Island, Central Philippines, whose runout distance about 3.8 km was enhanced by friction reduction due to undrained loading when the debris encountered colluvium and flooded paddy fields in the valley bottom (Evans et al., 2007) (Fig. 1b). Another case is the Oso landslide in Washington, USA, on 22 March 2014, which is situated in the North Fork Stillaguamish River valley (Wartman et al., 2016; Yerro et al., 2019) (Fig. 1c). In this case, hundreds of transient sand boils were identified, indicating that elevated pore-water pressure conditions were widespread during basal erosion of the slide (Collins and Reid, 2019). These cases highlight the significance of landslide-material interaction in understanding and predicting landslide runout.

Such material interactions cannot be overlooked in the runout assessments of landslides in alluvial basins, especially for large-volume landslides. These interactions, from material impact to shear, involve complicated physical processes and are influenced by multiple factors. These factors include geomorphological parameters, such as landslide volume (Okura et al., 2000; Larsen et al., 2010), slope inclination angle, and the thickness of the erodible bed (Iverson and Ouyang; Mangeney et al., 2010), as well as the internal geomechanical properties of the involved materials, such as water content or degree of saturation (Iverson et al., 2015; Liu et al., 2015), dilatancy that influences the pore pressure generation during landslide motion, fragility and shear strength that determines spreading of materials (Pudasaini and Krautblatter, 2021; Pudasaini et al., 2024), and permeability, which determines how long the elevated pore pressure can be sustained (Vicari et al., 2025; Zhu et al.). These studies show that quantitatively modelling material interactions during landslide motion is highly challenging, both theoretically and numerically, and remains a very active research topic (Bouchut et al., 2008). Especially in alluvial basin settings, slope transitions between the basin margins and the basin floor are typically abrupt rather than gradual, which amplifies the impact effects exerted by the landslide mass. This highlights the importance of placing more emphasis on quantitatively investigating impact interactions, which commonly occur together with erosion processes (Wang et al., 2014).

In this study, we quantitatively examined the Luanshibao landslide (Fig. 1d), a prominent example of a long-runout landslide, which represents a giant prehistoric hazard that occurred in a high-elevation alluvial basin. The distinctive morphological traits, coupled with the landslide's potential threat to nearby highway and railway lines, have attracted considerable research attention.

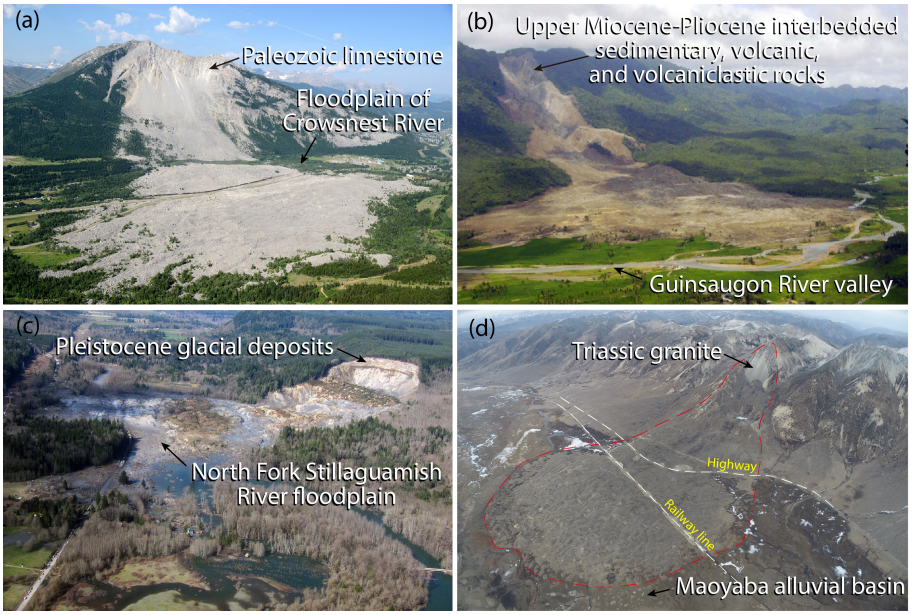


Figure 1. Typical examples of long-runout landslides characterised by material interaction. (a) The Frank Slide traveled about 2 km covering the floodplain of Crowsnest River (image from the Frank Slide Interpretive Centre); (b) Leyte rockslide-debris avalanche with great runout distance due to undrained loading in the valley bottom (Evans et al., 2007); (c) The Oso landslide, which accelerated across the floodplain of the North Fork Stillaguamish River (Reid, 2017); (d) The Luanshibao landslide in the Maoyaba Basin, involving extensive entrainment of alluvial sediment.

Some image-based deformation analyses have revealed that the source area of the landslide continues to undergo gradual deformation, with an annual surface displacement rate ranging from 15 to 20 mm/yr (Shi et al., 2021; Wang et al., 2023). Previous research on the Luanshibao landslide has primarily focused on three aspects: triggering factors, occurrence time, and movement mechanism. (1) Triggering factors: Given the substantial volume of the Luanshibao landslide, estimated to be $0.64 \sim 0.94 \times 10^8$ m^3 (Ren et al., 2021; Zeng et al., 2020), most scholars attribute its initiation to an earthquake along the Maoyaba fault, which intersects the landslide's source area (Guo et al., 2016, 2023; Zhang et al., 2022). (2) Occurrence time: Radiocarbon and ^{10}Be exposure-age dating have been used to assess paleoseismicity of the Maoyaba fault. By synthesising these results, the landslide's occurrence time can be narrowed to between 3,385 and 3,248 a. BP (Ren et al., 2021; Zeng et al., 2020; Zhao et al., 2020). Additional findings suggest that the Luanshibao landslide may have experienced two movement events: the first around 3.7 ka. BP and the second around 2.1 ka. BP (Zhao et al., 2021). (3) Runout mechanism: For understanding its high mobility, several hypotheses have been proposed. These include a "laminar-flow pattern" in alluvial sediments induced by earthquake liquefaction (Zeng et al., 2020), frictional heating effects within the sliding zone, and the presence of saturated sand layers in the Maoyaba Basin, which may have facilitated the long runout (Zhu et al., 2022).

All these aspects of the Luanshibao landslide make it a particularly interesting case for studying the mechanisms of landslides in alluvial basins. Thus, the dynamic characteristics of the landslide deposit are analysed and presented based on comprehensive

field investigations. A potential motion pattern, divided into an impact phase and a runout phase, is proposed to describe and present as the typical landslide motion behaviour in alluvial basins. To elucidate the mechanical mechanisms underlying the impact phase, impact-loading ring-shear tests were conducted on sandy sediment samples. For the runout phase, numerical simulations using the Material Point Method (MPM) were employed to explain the extended travel distance of the landslide. This was followed by an extended analysis to systematically explore how material parameters determine different landslide motion patterns. The findings of this study reveal a potential mechanism that may govern long-runout landslides in alluvial basin settings. This mechanism not only contributes to a better understanding of long-runout landslide dynamics in similar topographies, but also provides valuable insights for improving landslide runout prediction and mitigation strategies.

2 Characteristics of the Luanshibao landslide

The Luanshibao landslide is an ancient long-runout landslide that occurred at the boundary of the Maoyaba Basin, located in the southeastern marginal area of the Tibetan Plateau (30°11’48"N, 99°55’51"E) (Fig. 2a). Despite being an ancient event, its boundary remains distinctly visible, characterised by an ideally flat-spread morphology within the basin. The landslide’s depositional features are remarkable, including transverse and longitudinal ridges (Wang et al., 2018), a hummocky landscape (Dai et al., 2019), and X-shaped troughs (Wu et al., 2023). From the high-resolution digital surface model (DSM) model of the landslide (Fig. 2b), these distinct morphological features provide direct evidence of the dynamic impact process. The ridged area at the foot of the hill shows prominent transversal ridges, indicating the longitudinal compression during the impact. Following this, the landslide mass propagated and spread across the basin floor. Under the influence of tensional spreading forces, the deposits eventually developed into a hummocky morphology.

The longitudinal profile of the Luanshibao landslide show an extremely low angle of rest (Fig. 3a). The main movement direction is 203° south-westward. Based on the DSM, the total area of the landslide is calculated as about 4.316 km^2, with the depositional area accounting for approximately 75%, 3.272 km^2. The elevations of the landslide crown and toe are 4,857 and 4,093 m, respectively, resulting in a maximum height difference of 764 m. The maximum width of the landslide in the depositional area reaches 2,047 m, and the maximum horizontal sliding distance is about 3,850 m. Based on the inclination feature of the exposed main scarp, it can be inferred that the landslide initially dropped along a 36.4° slope. After impacting the slope-front sediment, the landslide maintained extremely high mobility and travelled a distance of 2,250 m on the flat basin plain. The overall apparent friction angle is 11.7°, while that in the depositional area is only 0.9°, which indicates the landslide’s high mobility. These features raise the questions of why the Luanshibao landslide has such a high mobility and what role the interaction between landslide mass and alluvial sediment plays in determining the impressive runout.

The Luanshibao landslide is located in a region where the geological conditions are simple. The source area is composed primarily of biotite granite, while the depositional area lies within an alluvial basin characterised by a dense network of more than 20 tributary rivers converging into the Litang river. The Luanshibao landslide deposit rests directly on the abundant basin sediment (Fig. 4a), indicating direct interaction between the sliding mass and the underlying alluvium. Although the main

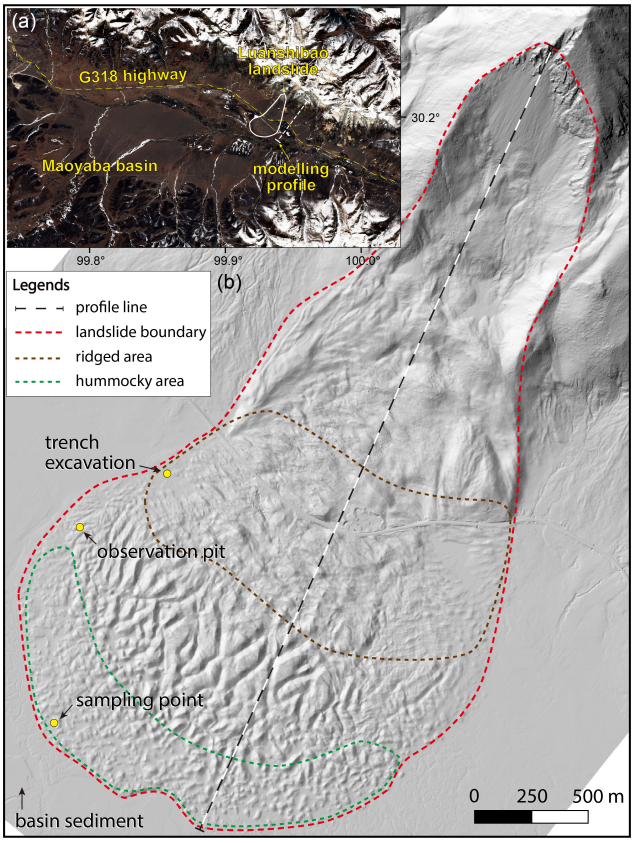


Figure 2. Plain view of the Luanshibao landslide. (a) Location of the Luanshibao landslide within the Maoyaba basin; (b) High-resolution DSM displayed in hillshade (generated from drone-based oblique photography at a resolution of 0.3 m).

scarp has gradually become covered by weathered granite debris over the long period since the landslide occurrence, it remains clearly identifiable in the landscape (Fig. 4b).

A trench was excavated to investigate the internal structure of the landslide deposits (location marked in Fig. 2). The trench profile, located near the right boundary of the landslide close to the highway, reveals that the interface between the landslide material and the underlying sediment is no longer distinguishable because of their similar mineral composition and the effects of long-term post-depositional processes. As a result, the profile can only be divided into two visually distinct layers. The top layer consists of humus soil, approximately 0.2 m thick, which provides nutrients for the basin's grassland. The lower layer, which is inferred to control the runout mechanism, is composed of thick, homogeneous sandy soil, consistent with the composition of the basin sediment. An observation pit was further excavated along the landslide boundary to investigate the groundwater conditions within the landslide area (location marked in Fig. 2). As shown in Fig. 4c, the groundwater surface was exposed after removal of the overlying humus soil, indicating that the groundwater level here is extremely shallow.

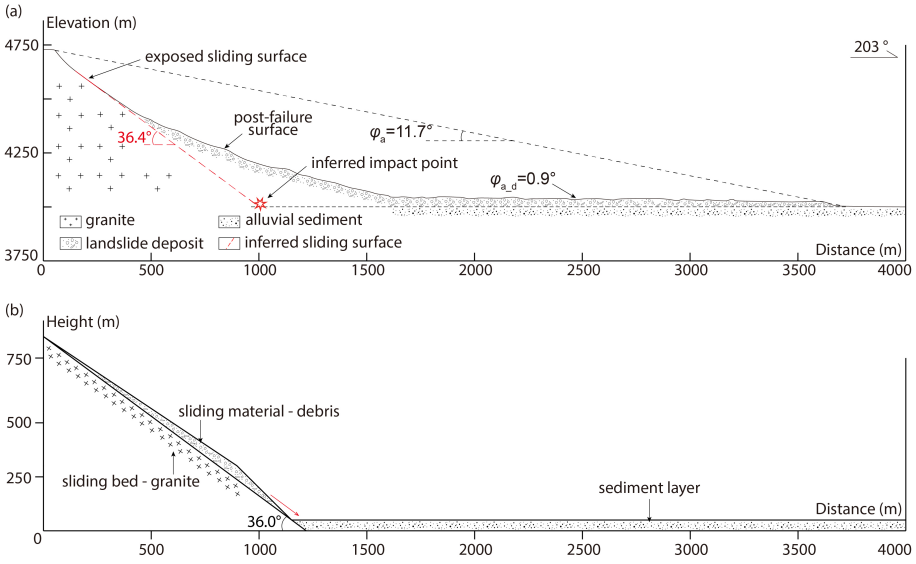


Figure 3. Cross-sectional profiles of the Luanshibao landslide. (a) Longitudinal cross-section of the landslide area showing key kinematic features; (b) Geometry of the numerical model cross-section constructed from an adjacent unfailed slope.

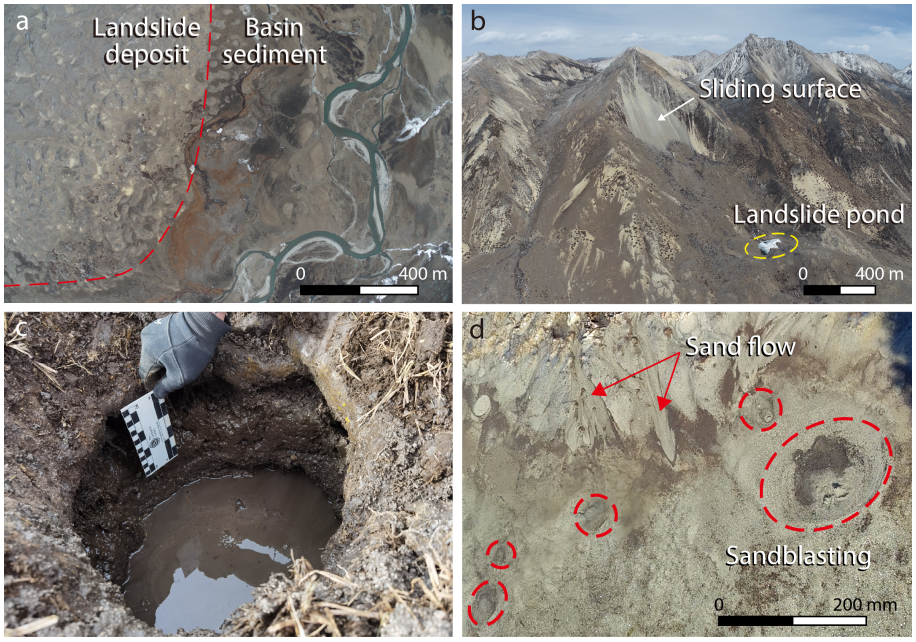


Figure 4. The Luanshibao landslide's geological and hydrogeological features. (a) Aerial photo shows the direct contact boundary of the landslide deposit and alluvial sediment; (b) A frozen landslide pond on the upper part of the landslide, indicating the hydraulic head difference within the landslide mass; (c) Shallow groundwater surface exposed after removal of 0.2 m humus soil layer; (d) Sandblasting formed craters at the front edge of the landslide.

In addition to the shallow groundwater table observed in the pit, parts of the landslide deposit exhibit signs of localised pressurisation. Sandblasting phenomena are widely observed in the alluvial sediment near the front edge of the landslide, where fine-grained sandy layers are intermittently ejected by water pressure at intervals of several metres, forming small 'craters' (Fig. 4d). This indicates that the alluvial sediments in certain areas of the Maoyaba Basin are under conditions with elevated pore water pressure. The phenomenon is especially pronounced along the landslide boundary and is most likely attributed to the presence of numerous water ponds distributed across the landslide area. These ponds suggest substantial groundwater seepage from the surrounding slopes, driven by the hydraulic head differences within the basin. Among them, the largest pond is located at the head of the landslide, with its surface frozen during the day of investigation (Fig. 4b). The high permeability of the granitic sandy materials, combined with the region's frequent freeze-thaw cycles and abundant precipitation, facilitates groundwater accumulation and the formation of a confined sediment layer within the basin, which provided a special erosive media for influencing the landslide runout.

3 Materials and Methods

This study is grounded in the analysis of the kinematic features of the Luanshibao landslide obtained from field investigations. These investigations included the establishment of a drone-based DSM, trenching within the landslide deposit, and material sampling in the erosive layer. To discuss the impact and erosion effects of the landslide motion separately, we conceptualised the motion after initiation as comprising two phases: the impact phase occurring at the slope foot and the runout phase taking place across the flat basin. For the impact phase, impact-loading ring-shear tests were carried out to examine the responses of pore water pressure and shear strength under varying levels of dynamic impact. Subsequently, numerical simulation were conducted via MPM for both impact and runout phases to elucidate how the variations in material properties influence the impact process, leading to different runout characteristics. A more detailed description of methodologies and parameters employed is provided in the following sub-sections.

3.1 Impact-loading tests in undrained ring-shear

Impact-loading ring-shear test is used to geotechnically simulate the soil behaviour impacted by dynamic normal and shear stresses. Fig. 5a shows a conceptual model of a landslide impacting the basin material, and Fig. 5b presents the corresponding theoretical stress path of the impacted specimen during this process. Considering a block of sliding mass detaching from an elevated slope, the runout process can be divided into three stages, including the initial stage, the impact stage, and the sliding stage. Taking an element at the rupture surface within a unit soil column for force analysis, in the initial stage, the sediment is subjected to gravitational load determined by its buried depth h_0, bulk unit weight γ, and dip angle of the basin surface θ, which is normally small. As the sliding mass descends from a higher elevation, it imposes an impact force P_d on the sediment surface along the direction of the sliding surface, which has an angle α with the basin floor. This force induces increases in normal and shear stresses through stress propagation within the sediment layer. In the laboratory tests, this process is simplified by applying a dynamic normal stress $\Delta\sigma_\mathrm{d}$ and a dynamic shear stress $\Delta\tau_\mathrm{d}$ to the specimens, thereby mimicking the effect of

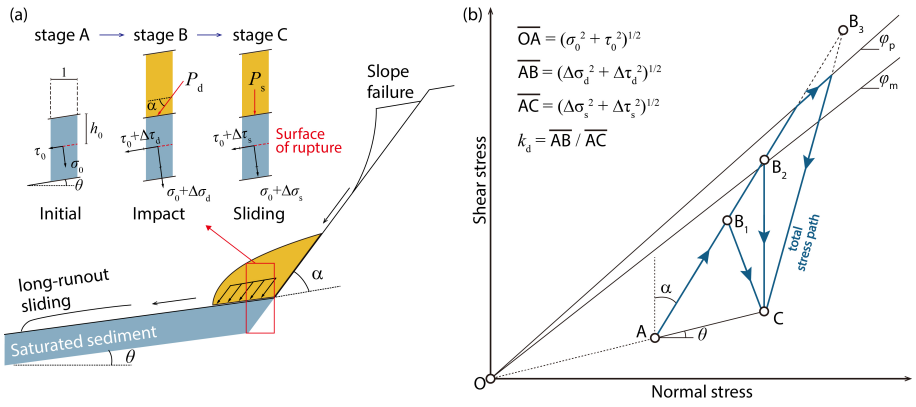


Figure 5. Schematic diagram of the landslide impact effect discussed in this study. (a) Three-stages model of landslide impact-runout process (h_0 denotes the assumed burial depth of the rupture surface within the sediment layer; α denotes the angle between the initial sliding surface and the sediment surface; θ denotes the slope angle of the sediment layer); (b) Theoretical stress paths of the impact-loading ring-shear tests (modified from Sassa et al. (2004)) (φ_p denotes the peak friction angle; φ_m denotes the mobilised friction angle). Note that θ is not necessarily identical in figures (a) and (b), as the slope of the rupture surface within the sediment layer may differ from the sediment surface slope in real cases.

the impact load. In the sliding stage, the sliding mass progressively disintegrates and continues to slide along the basin surface until final deposition, at which point the accumulated material exerts an additional static load P_s due to its self-weight on the underlying sediment. This loading is also simplified in the tests as additional stress components, expressed as $\Delta\sigma_s$ and $\Delta\tau_s$.

The stress paths in Fig. 5 show the stress state transitions among these stages, illustrating the mechanical features such as shear resistance and pore water pressure of the sediment specimens in response to the impact load. The total stress path, depicted in blue, starts at point A (initial stage), rapidly transits to point B (extreme stress state during the impact stage), and ends at point C (the beginning of the sliding stage, while the specimen may keep shearing under a very small driving force due to its low shear resistance). Line AB, which has an angle α with the vertical direction, represents the stress increase caused by the impact load, that is $\Delta\sigma_d = |\boldsymbol{AB}| \times \sin\alpha$ and $\Delta\tau_d = |\boldsymbol{AB}| \times \cos\alpha$. Line AC, with a slope of θ, signifies the stress change caused by the weight of a unit column of overlying material between the initial and final stages, that is $\Delta\sigma_s = |\boldsymbol{AC}| \times \cos\theta$ and $\Delta\tau_s = |\boldsymbol{AC}| \times \sin\theta$.

Considering the theorem of impulse, the magnitude of impact load is controlled by the velocity of the sliding mass and the duration of impact. In reality, this impact magnitude cannot be inferred simply from height difference and volume. It also depends on landslide material properties, including rock or soil types, fragility, brittleness and so on, which strongly influence both the impact effect and subsequent runout behaviour. In the ring-shear tests, based on the peak value of the impact load, the loading path can be presented in three different ways: line AB_1C, line AB_2C, and line AB_3C. These correspond to three different positions of the peak stress state relative to the failure lines: point B_1 lies below the mobilised failure line, point B_2 between the mobilised and peak failure lines, and point B_3 above the peak failure line. Each case exhibits a different unloading

Table 1. Experimental conditions for impact-loading tests in ring-shear

No.	k_d	mid-time normal stress (kPa)	mid-time shear stress (kPa)	final normal stress (kPa)	final shear stress (kPa)
1	1.0	216	165	300	6
2	1.7	300	280	300	6
3	2.5	390	410	300	6

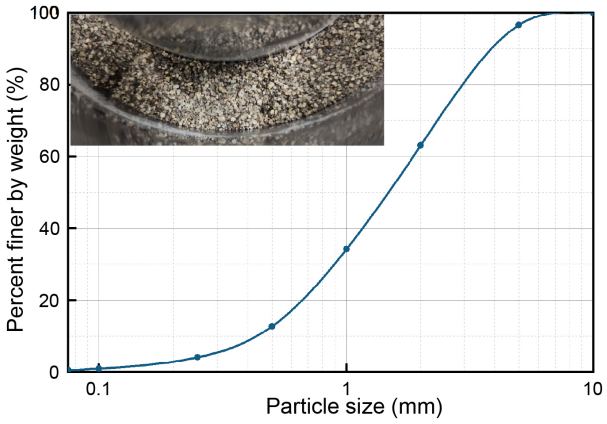


Figure 6. The LSB sand sample and its grain size distribution curve

path, where the normal stress either increases or decreases after the impact peak, affecting shearing behaviour during the following sliding stage. To quantify these impact modes, we introduced the dynamic coefficient (k_d) as the ratio of impact pressure magnitude to static pressure magnitude as $k_d = |\boldsymbol{AB}|/|\boldsymbol{AC}|$ (Sassa et al., 2004).

In this study, we used three different levels of k_d in the ring-shear tests with a fixed impact duration of 5 s. The load parameters used are listed in Table 1. Undrained condition is employed, because the rapid process of the landslide impact does not give sufficient time for pore pressure dissipation. The ICL-2 ring-shear apparatus (Sassa et al., 2014) was employed. This apparatus is capable of maintaining undrained condition during dynamic shearing and able to provide theoretically infinite shear distance, making it particularly suitable for investigating the rapid mechanical response of shear zone material during landslide processes. The samples, named LSB sand (Fig. 6), were collected from the alluvial sediment layer in the excavated trench in the landslide depositional area. All the tests were performed under saturated conditions (The process of specimen preparation is described in detail in the Appendix A). Basic physical and mechanical properties of LSB sand were tested in accordance with Chinese Geotechnical Testing Standards (GB/T 50123-2019). The results of these tests are summarised in Table 2.

Table 2. Physical parameters of the LSB sand sample

Physical parameters	LSB sand
Limiting particle size D_{60} (mm)	1.876
Average particle size D_{50} (mm)	1.469
Effective particle size D_{10} (mm)	0.411
Uniformity coefficient C_u	4.564
Specific gravity G_s	2.699
Maximum void ratio e_{max}	1.222
Minimum void ratio e_{min}	0.425

3.2 Impact-runout modelling by material point method

To further investigate how the duration of materials interaction, which is influenced by the material properties, controls both the impact and following runout processes, numerical simulations were conducted to quantitatively describe the entire runout process under different scenarios. Since Luanshibao landslide is an ancient case, it is difficult to precisely reconstruct the post-failure topography. Therefore, the model geometry (Fig. 3b) was established using the cross-sectional profile of an unfailed slope adjacent to the Luanshibao landslide (profile line is depicted in Fig. 2). The model has a total height of 850 m and includes a 50 m thick sediment layer. The slope of the sliding surface is 36°, consistent with the exposed surface of rupture.

Based on the observations that groundwater level was extremely shallow in the landslide area and to simplify the model, the materials used in the simulations except for the bedrock were all considered under saturated condition. For this case, a two-phase MPM for saturated soil framework was used (Community, 2022). This framework follows the mixture theory that uses porosity to divide the contents of solid and liquid, and the porosity update was not manually controlled through the simulations but derived based on the evolution of material volume temporally and spatially. This framework describes the coupling problem with four equations, in which the subscript 's' stands for the solid phase and 'l' stands for the liquid phase. They are two conservation equations for the mixture (Eq. 1 and 2), one momentum equation for the liquid (Eq. 3), and one equation for the solid skeleton, depending on the choices of linear elastic model or Mohr-Coulomb model in this study.

$$\frac{d(\overline{\varepsilon_L})}{dt} = \frac{1}{n}\left[(1-n)\nabla \cdot \mathbf{v}_S + n\nabla \cdot \mathbf{v}_S\right] \tag{1}$$

$$(1-n)\rho_S \frac{d\mathbf{v}_L}{dt} + n\rho_L \frac{d\mathbf{v}_L}{dt} = \nabla \cdot \boldsymbol{\sigma} + \rho_{sat}\mathbf{g} \tag{2}$$

$$n\rho_L \frac{d\mathbf{v}_L}{dt} - n\nabla p_L - n\rho_L \mathbf{g} + \frac{n^2 \rho_L g}{k}(\mathbf{v}_L - \mathbf{v}_S) = 0 \tag{3}$$

Table 3. Material parameters adopted in the impact-runout simulations.

parameters	sliding mass	erodible sediment	bedrock
material type	weathered granitic debris	alluvial sediment	granite
constitutive model	Mohr-Columb (undrained)	Mohr-Columb (fully coupled)	linear elastic
initial porosity	0.2	0.6	0.0
solid density (kg/m^2)	2699	2699	2699
liquid density (kg/m^2)	1000	1000	-
intrinsic permeability (m^2)	-	$1 \times 10^{-12} \sim 1 \times 10^{-9}$	-
effective Poisson's ratio	$0.25 \sim 0.40$	$0.25 \sim 0.40$	0.25
effective Young's modulus (kPa)	$1 \times 10^4 \sim 1 \times 10^5$	$1 \times 10^4 \sim 1 \times 10^5$	4×10^7
effective friction angle (degree)	34	34	0

In those equations, ε_L is the effective volumetric strain, n is the porosity of the mixture, $\mathbf{v}$ is the velocity vector, ρ is the density, $\mathbf{g}$ is the gravitational acceleration, and k is the isotropic Darcy permeability which is controlled by intrinsic permeability and viscosity of the liquid in the simulations.

In this study, the base of the slope described in Fig. 3b was considered to be consist of granite bedrock, described by a linear elastic model. Both the sliding material and the erosive sediment layer are described using Mohr-Coulomb model, with effective friction angle determined from the prior monotonic ring-shear tests (see Appendix for details). The sliding material is considered as weathered granitic debris which should be relatively denser than the erosive layer that primarily composed of loose alluvial sediment. Based on the hydrogeological features from field observation (introduced in Section 2), both materials are modelled as in a saturated state. To comprehensively evaluate the influence of material properties on landslide impact and the following runout patterns, two parameters of both sliding material and erosive sediment, including Young's modulus E and Poisson ratio ν, are varied and tested to see how the stiffness and compressibility of materials contribute to the impact depth, velocity, and final runout. The numerical simulation scenarios and the corresponding parameter values are list in Table 3.

4 Results

Based on the field observation described above, a key unresolved question is: why did this landslide exhibit such high mobility? This uncertainty also raises our interest in understanding the role of pore pressure within the erodible sediment. In addition to water, are there other factors influencing the interaction between the landslide mass and the alluvial sediment that might account for variations in mobility and runout behaviour? A quantitative explanation is essential for answering these questions. Building on the previous analysis of the landslide's kinematic characteristics, we conducted a series of physical and numerical experiments to investigate the effects of impact-induced interaction on long-runout landslides in similar basin environments. The results of these experiments are presented in detail below.

4.1 Shear resistance behaviour in the impact-loading ring-shear tests

The ring-shear tests began with monotonic shear tests to evaluate the fundamental strength properties of the material (described in detail in the Appendix). Under fully drained conditions, the mobilised friction angle of the sample was found to be approximately 34°, and this value was subsequently used to plot the failure lines in the following tests. Under undrained conditions, the maximum excess pore water pressure ratio r_u, defined as the ratio of pore water pressure generated during shearing to the total normal stress, stabilised at approximately 0.83 after a shearing distance of 1,000 mm. This value represents the liquefaction potential of the LSB sand under monotonic shearing conditions. For comparison, Fig. 7 presents the results of impact-loading ring-shear tests conducted under three different dynamic coefficients. Figs. 7a-c display the applied impact signals corresponding to k_d values of 1, 1.7, and 2.5, respectively. All samples were consolidated under the same initial stress conditions, simulating a depth of approximately 6 m within the sediment layer. In each test, the impact load comprised two stages: a loading stage from 10 s to 15 s, followed by an unloading stage from 15 s to 20 s. The loading modes can be categorized into three types, as described in the previous section, depending on whether the normal stress pulse increases, decreases or remains stable after reaching the peak stress at 15 s.

Figs. 7d-f present the results of these tests in stress path space. The Total Stress Path (TSP) is shown in black, while the Effective Stress Path (ESP) is shown in red. At the beginning of each test, both TSP and ESP initially move upward together, starting from 100 kPa in normal stress and 2 kPa in shear stress, in response to the applied impact load. Shortly afterwards, pore water pressure begins to build within the specimens, causing the TSP and ESP to diverge. In the test with a dynamic coefficient k_d=1.0, the ESP quickly touches the failure line but then moves downward, entering a more stable state due to a combination of decreasing shear stress and increasing normal stress during the unloading stage. In contrast, for k_d=1.7 and k_d=2.5, the ESP continues to follow the failure line after initial contact, eventually driving the specimens into a fully liquefied state. Figs. 7g-i illustrate the temporal evolution of total normal stress, shear stress, pore water pressure, and shear displacement during these tests. Under k_d=1.0, the sample undergoes only a few millimetres of displacement during the impact stage. As the test transitions into unloading, the normal stress continues to rise, quickly halting further motion. The final excess pore water pressure ratio r_u stabilises at approximately 0.74, indicating that under this condition, the impact load was insufficient to generate the pore pressure required to trigger long-runout motion. In contrast, for k_d=1.7 and k_d=2.5, the excess pore water pressure ratios exceed the value of liquefaction potential identified under monotonic shearing. Unlike the monotonic tests, these samples experience complete strength loss, and the resulting motion continues without interruption. Interestingly, under k_d=1.7, it takes roughly 20 s for the sample to reach complete strength loss, while it takes about 60 s for k_d=2.5. This observation indicate that an optimal level of impact stress may exist that maximises the liquefaction efficiency within the erodible layer.

4.2 Variable runout patterns in the numerical simulations

The simulations of the impact and runout phases were performed using a two-dimensional cross-sectional model, beginning with a benchmark case. In this benchmark scenario, the Young's modulus is set to 1×10^4 kPa for the landslide mass and 1×10^5 kPa for the sediment layer, while Poisson's ratio is fixed at 0.35 for both materials. These parameter choices reflect

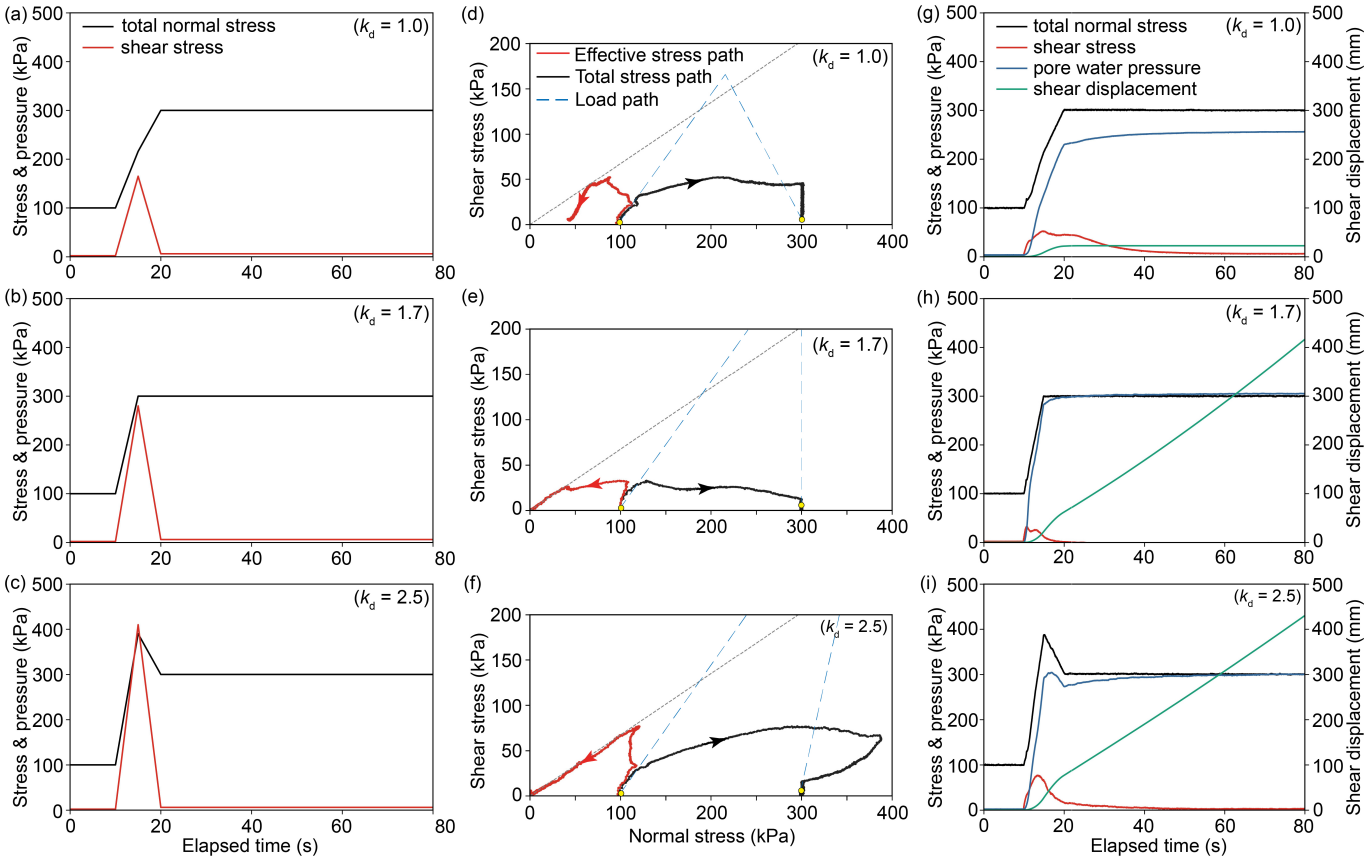


Figure 7. Results of impact loading tests. (a-c) Input signals of the impact loading modes; (d-f) Actual response of the stress line under impact loading; (g-i) Mechanical response versus elapsed time under the impact loading.

the geological context of the Luanshibao landslide, treating the landslide mass as fractured granitic gravel and the underlying sediment as sandy soil. All subsequent simulations, involving various combinations of material properties, are compared to this benchmark to investigate their influence on the impact dynamics and runout behaviour. Fig. 8 shows the displacement field throughout the process, illustrating the interaction between the sliding mass and the saturated erodible sediment. After initial failure, the landslide mass descends along the granitic sliding surface and impacts the sediment layer. Upon impact, the sliding mass penetrates approximately 10 m into the sediment, entraining sediment material into the moving body. This entrainment promotes continued forward motion across the relatively flat topography of the alluvial basin, effectively reproducing the long-runout pattern observed in the Luanshibao landslide. Fig. 9 illustrates the evolution of excess pore water pressure during the impact-runout phase. Excess pore water pressure is generated almost instantaneously at the moment of impact, particularly near the slope toe in both the upper and basal zones of the landslide. This pressure continues to evolve as the landslide progresses, forming a low-friction basal layer that facilitates sustained motion.

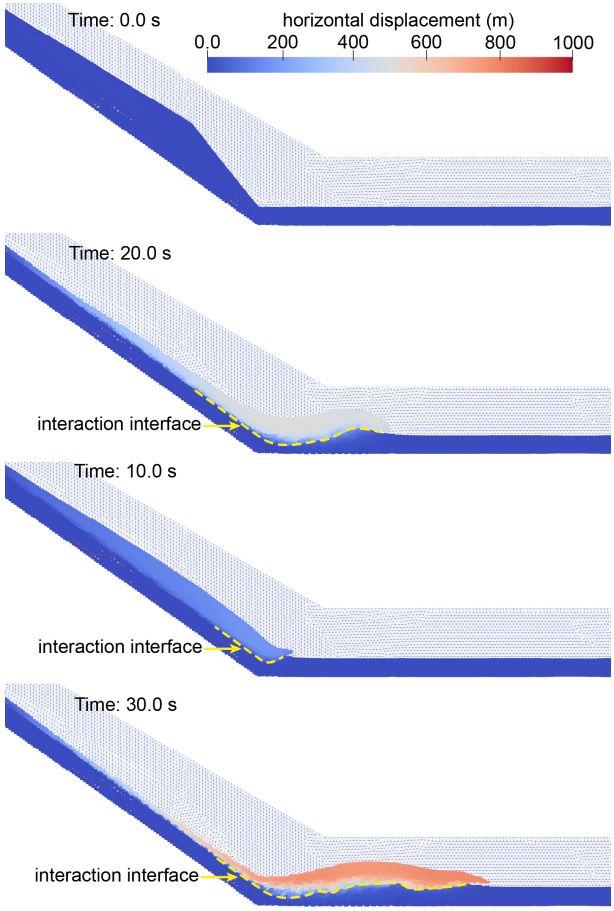


Figure 8. Simulation result of the benchmark scenario shown in the horizontal displacement field

To investigate the influence of material properties in both the sliding mass and the erodible sediment layer, a series of comparison simulations were conducted by varying the Young's modulus (from 1×10^4 to 1×10^5 kPa) and Poisson's ratio (from 0.25 to 0.40). The results indicate that even slight changes in these parameters can lead to significant variations in landslide mobility and deposition patterns. Fig. 10 presents polynomial-fitted curves illustrating how landslide mobility, represented by final sliding distance, and impact depth, respond to changes in these parameters. As shown in Figs. 10a and 10b, increasing the stiffness of the sliding mass leads to a noticeable reduction in mobility, accompanied by a significant increase in impact depth. In contrast, increasing the stiffness of the erodible sediment layer results in only a slight increase in mobility up to a modulus of approximately 7×10^4 kPa, after which the mobility plateaus. Meanwhile, the impact depth shows a sharp decline with increasing stiffness of the sediment layer. Figs. 10c and 10d indicate that the variations in the properties of the erodible sediment have limited influence on overall landslide dynamics. However, decreasing the compressibility of the sliding mass leads to a marked decrease in final runout distance. Interestingly, the impact depth exhibits a hyperbolic trend with respect to Poisson's ratio, reaching a minimum near a ratio of approximately 0.31. In summary, stiffness and compressibility exert

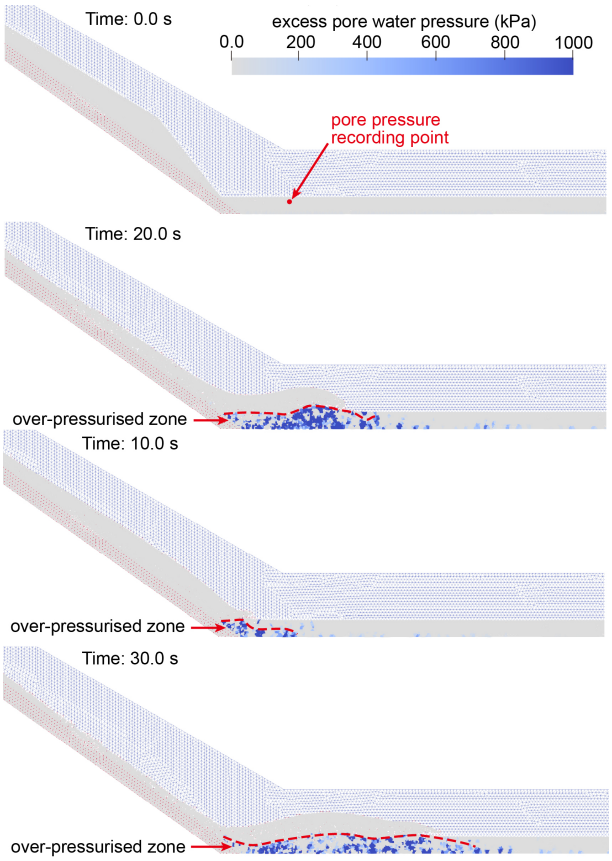


Figure 9. Simulation result of the benchmark scenario shown in the pore water pressure field

opposing influences on impact and runout behaviours in the two materials, except that the effect of Poisson's ratio on impact depth appears to follow a non-monotonic pattern.

Here, we highlight two simulation cases that exhibit the most distinct runout behaviours compared to the benchmark scenario. Fig. 11a presents the case in which the sliding mass has a higher Young's modulus of 1×10^5 kPa. In this scenario, a stiffer landslide mass transfers most of its momentum into penetrating the sediment layer, reaching an impact depth of approximately 40 m. Instead of entraining sediment material, the stiff mass pushes it forward, forming a barrier in front of the landslide that hinders further motion. By contrast, a markedly different behaviour is observed when the sliding mass exhibits higher compressibility, as shown in Fig. 11b for a Poisson ratio of 0.25. In this case, the sliding mass disintegrates upon impact with the sediment surface, resulting in a shallower impact depth of approximately 31 m. Although the amount of entrained sediment is moderate, entrainment prevails over penetration as the dominant interaction mechanism, enabling the landslide to bypass barrier formation and maintain its forward movement. These contrasting outcomes suggest that the stiffness and compressibility of both the sliding mass and the alluvial sediment play critical roles in governing the dynamics of impact interaction and the subsequent runout pattern.

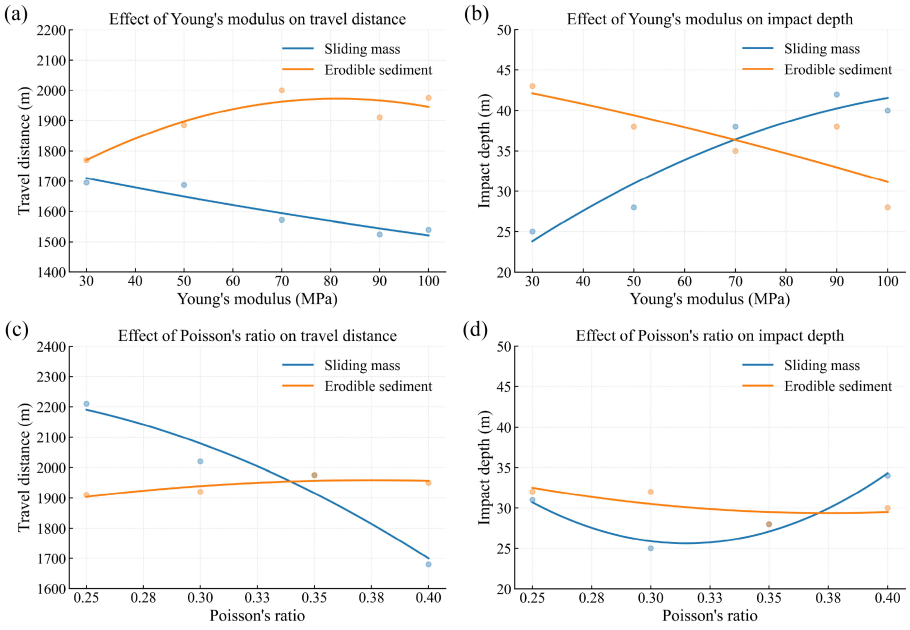


Figure 10. Influence of elastic parameters on the dynamic interaction between the sliding mass and erodible sediment. (a) Final travel distance influenced by Young's modulus; (b) Final travel distance influenced by Poisson's ratio; (c) Impact depth influenced by Young's modulus; (d) Impact depth influenced by Poisson's ratio. In each simulation scenario, all parameters other than the one being varied are kept identical to those in the benchmark case.

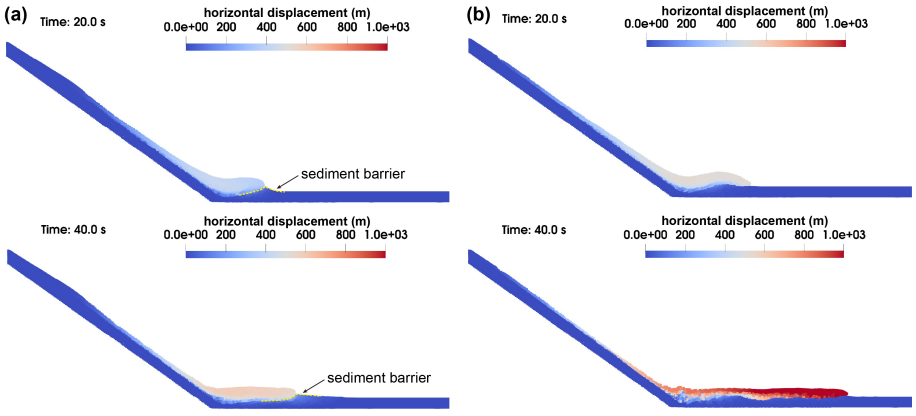


Figure 11. Two possible runout patterns caused by different material properties. (a) A stiffer sliding mass with Young's modulus of 1×10^5 kPa; (b) A more deformable sliding mass with a Poisson's ratio of 0.25.

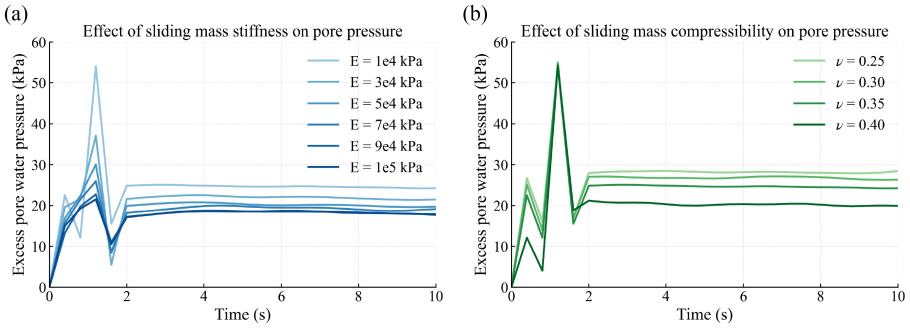


Figure 12. Pore pressure response under varying impact duration determined by elastic parameters. (a) Excess pore pressure response at a representative material point subjected to impacts from sliding masses with different stiffness values; (b) Excess pore pressure response at the same point for sliding masses with different compressibility.

These analysis shows that variations in the elastic parameters of the materials involved in the landslide impact process significantly influence landslide mobility, primarily through their control on impact duration. To quantitatively examine the pore pressure response under different impact situations, we select a material point located in the shallow layer of the erodible sediment near the impact region (initial coordinates: (1400, 40). The excess pore pressure responses are presented in Fig. 12. As shown in Fig. 12a, a less stiff impactor generates higher excess pore pressure. This is attributed to the fact that a stiffer material shortens the impact duration, leading to a more impulsive interaction. Fig. 12b shows that the pore pressure response is less sensitive to the variation of Poisson's ratio in terms of peak values. However, it can still be observed that increasing the compressibility of the sliding mass reduces the minimum pore pressure values during the process. It should be noted that the selected material point moves during the simulation. Therefore, the recorded data does not correspond to a fixed spatial location and can not fully represent the spatial variability of the pore pressure field. Nevertheless, it still provides useful information of the sensitivity of the modelled system.

5 Discussions

Long-runout landslide patterns similar to the Luanshibao landslide are commonly observed in alluvial basins and floodplains located in high-elevation regions. These areas are characterized by frequent faulting and seismic activity, which can trigger internal failure within high-elevation rock masses; relatively young rock exposure ages in landslide source areas, often associated with brittle mechanical behaviour; extremely thin weathered layers covering steep slopes; and the accumulation of loose, highly saturated materials, including alluvial sediment, landslide debris, and glacial moraines in adjacent low-lying basins. Material released from elevated positions tends to travel over bare rock slopes with minimal energy loss, making the impact interaction at the slope foot a non-negligible process. Given these conditions, it is crucial to explore impact mechanisms for the purpose of a more accurate runout assessment. This impact process involves the disintegration of the sliding mass and modifies the mechanical behaviour of the underlying materials. Specifically, changes in pore water pressure, shear strength, and basal

friction during impact significantly influence landslide mobility. Therefore, a detailed investigation of how material properties govern the mechanical response and the ultimate runout pattern is essential.

In the context of high-elevation landslides occurring in alluvial basins, erodible sediment - potentially incorporated into the landslide mass through material interactions - can experience higher excess pore water pressure under impact conditions than under monotonic rapid shearing. This elevated pore pressure is likely attributable to the impact-induced disruption of the sediment's initial consolidated structure, thereby increasing its susceptibility to liquefaction. According to the theorem of impulse, the change in the impactor's momentum is equal to the product of the impact force and the impact duration, while the magnitude of the impact load depends on the landslide mass and its velocity at the moment of impact. For a given landslide geometry, the mass at impact is fixed. However, the impact duration and velocity are related to the initiation mechanism and propagation processes, where material properties play a significant role. To investigate the influences of material properties on the mechanical response of the sediment layer, we set a constant impact duration while varying the dynamic coefficient. This coefficient represents the level of impact load determined by internal material properties in real-world scenarios. The applied impact load can be classified into three modes, as illustrated in Fig. 5, distinguished by how the normal stress evolves after reaching its peak.

The results of ring-shear tests indicate that those different impact modes can lead to distinct soil responses in terms of effective stress path, as shown in Fig. 13. At the lowest impact level, the effective stress path only reaches the failure line and slightly drops back, and thus does not trigger a catastrophic slide within the specimen, as represented by path AD_1. The other two impact modes both eventually lead the specimen to a state of complete liquefaction, but through different mechanisms. A moderate impact tends to induce structure-related pore pressure generation, with the stress path AD_2 curving directly toward the origin. In contrast, a higher impact level initially destroy the soil structure, driving the path to the failure line and initiating shear deformation within the specimen. Subsequent pore pressure generation then causes the path evolve toward the origin along the failure line, as shown by path AD_3. These two failure modes present different liquefaction efficiencies, as structure-induced pore pressure generation occurs more rapidly than that associated with shear-induced grain crushing. This observation suggests that, in real landslide cases, the final mobility of the sliding mass is not solely positively correlated with the impact intensity, but is also strongly influenced by the failure mechanisms govern by the specific impact modes.

In the numerical simulations, we investigated the effect of impact duration on landslide mobility by indirectly varying materials properties. In addition to the two elastic parameters discussed previously, it should be acknowledged that other factors, such as material permeability and initial porosity, may also significantly affect landslide dynamics. To assess their potential roles, we also conducted a series of parallel simulations, in which the intrinsic permeability of the erodible layer was varied from $1 \times 10^{-10} \sim 1 \times 10^{-12}$ m^2, and the initial porosity was varied from 0.2 to 0.6. However, these variations did not produce pronounced changes in landslide mobility or runout patterns, particularly when compared with the sensitivity observed for the elastic parameters. This does not imply that these factors are unimportant in controlling landslide behaviour. Their influence appears to be less significant for the present case, likely due to the specific spatial scale and temporal duration of the simulated event. Their roles in modulating pore-pressure diffusion, impact dynamics, and erosion processes remain important topics for further investigation in more studies.

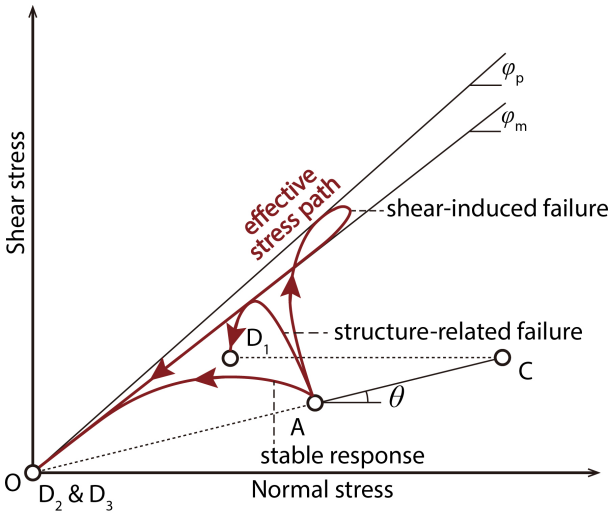


Figure 13. Effective stress paths for three impact responses induced by varying impact coefficient levels.

6 Conclusions

This study investigates the runout mechanisms of landslides in alluvial basins, highlighting the role of landslide impacts on saturated basin sediments in initiating erosion processes during runout. Taking the Luanshibao landslide as an example, numerous landslide ponds were observed in the landslide area, along with the widespread sandblasting phenomenon along the landslide boundary, indicating the active groundwater seepage within the landslide mass. This suggests that both the landslide material and the basin sediment were likely in a highly saturated state at the time of failure. The impact of failed high-elevation mass could generate excess pore water pressure that was difficult to dissipate promptly at the interface between the sliding mass and the underlying sediment. This excess pore water pressure at the sliding interface significantly reduced the basal friction and sustained long runout.

However, results from both ring-shear tests and numerical analyses reveal that the interaction between the impacting landslide mass and the basin sediment does more than simply extend the landslide's runout distance. Due to differences in landslide volume and in the properties of both the impactor and substrate, different motion patterns can emerge. The stiffness and compressibility of these materials strongly influence the peak impact force, which correspondingly alters the final runout distance and pattern. Loose and brittle landslide material tends to disintegrate upon impacting saturated sediments and travel farther over weak basal layers, while intact and stiffer masses penetrate sediments and lose mobility.

Such impact-induced processes should not be overlooked in mobility analyses, especially in alluvial basin environments characterised by abundant groundwater and sharp changes in slope angle at the basin boundary. The current omission of this impact factor in numerical models could lead to a misjudgment of hazard risks. Therefore, it is necessary to develop mathematical models that more precisely reflect the impact effect for the future improvement of landslide numerical simulations. In addition, recognising the significance of impact force levels and the properties of erodible materials can provide useful

guidance for researchers and practitioners working on risk analysis and mobility estimation. In particular, incorporating parameters such as slope angle changes and the mechanical state of regional materials may be necessary when conducting hazard assessments.

Data availability. The processed data and the raw test data are accessible through the ScienceDB depository in Chen (2025). The software for numerical simulation is Anura3D which is open access at https://github.com/Anura3D. For further inquiries, please contact the corresponding author.

Appendix A: Strength properties of the LSB sand derived from monotonic shear tests

The samples preparation process and the results of proceeding monotonic tests are introduced here. Tests were performed on the sediment samples under both shear rate-controlled and impact loading conditions in this study. All samples were loosely compacted into the shear box and consolidated under the specified stress. Firstly, drained tests were conducted to determine the internal friction angle of the sample at the critical state (also known as the mobilized friction angle, as it reflects the mechanical behaviour of the shear zone during landslide motion). In the drained test, the normal stress was modulated to change linearly while the sample is under shearing, allowing the mobilized failure line to be derived from the moving stress path. The mobilized friction angle of the sample was found to be approximately 34°.

After that, direct shearing and impact-loading tests were carried out on saturated samples under undrained condition. Each sample was first saturated using a method combining vacuuming and carbon dioxide displacement. The saturation degree was then verified using the B_{D} value, which is the ratio of the increase in excess pore water pressure to the applied normal stress. The B_{D} values of all samples in this study were confirmed to be above 0.95, indicating full saturation. Following the saturation process, the samples were consolidated under calculated normal and shear stresses, simulating the stress state related to gravitational forces in the initial rested stage. Once consolidation was complete, the next loading process commenced.

Fig. A1 illustrates the stress path of the shear rate-controlled tests. The dashed line in Fig. A1a represents the mobilized failure line. The data reveal that the LSB sand exhibited an increase in pore water pressure and a loss of strength after being sheared over a distance of 1000 millimeters under normal stresses of 300, 400, and 500 kPa. After sufficient shearing distance, the excess pore water pressure generated within the sample stabilized at a constant value. The results indicate that the maximum excess pore water pressure ratio achievable by the LSB sand is approximately 0.83. This final excess pore water pressure ratio is influenced by the mineral composition of the soil. The final apparent friction angle of the sand sample was reduced to only 2.2°, a condition that significantly facilitates the long-distance movement of the sliding mass. It is noteworthy that the LSB sand sample did not achieve complete liquefaction through monotonic shearing. Unlike vibration-induced liquefaction, the degree of shear liquefaction in sand samples depends on their mineral composition and particle size distribution.

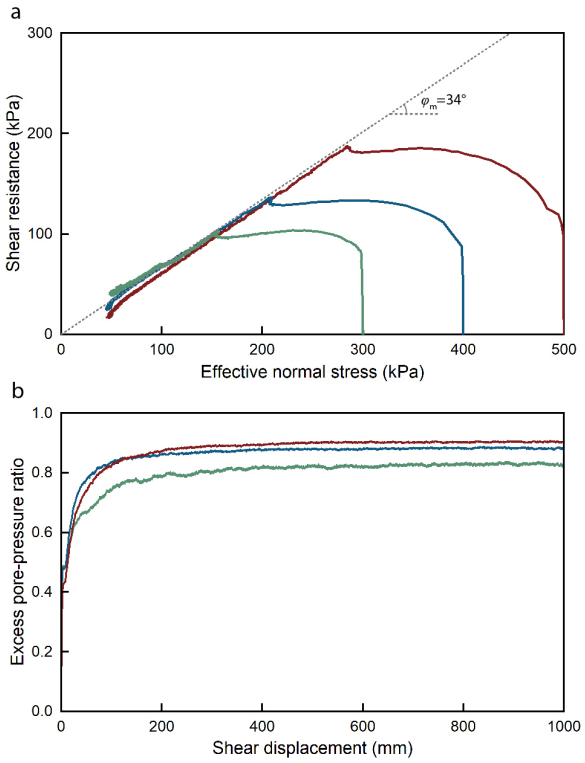


Figure A1. Strength properties of the LSB sand determined by monotonic rate-controlled shear tests. (a) Stress paths of undrained monotonic ring-shear tests on saturated specimens and the failure line. (b) Excess pore water pressure ratio in the monotonic shear tests.

Author contributions. YC designed and performed the physical and numerical experiments. FW acquired the funding, and together with MV provided supervision and conceptualisation for the study. WL, BZ, and CG assisted in data and sample collection during field investigations. YC prepared the manuscript with contributions from all co-authors.

Competing interests. The authors declare there are no conflicts of interest for this manuscript.

Acknowledgements. This study is supported by the Key Project of the National Natural Science Foundation of China (Grant No. 42230715), and the China Scholarship Council program (Project ID: 202406260107). The authors are sincerely grateful to the students from Tongji University, including Hao Ma, Zijin Fu, and Youqian Feng, for their kind support during the field investigation.

References

Bouchut, F., Fernández-Nieto, E. D., Mangeney, A., and Lagrée, P.-Y.: On new erosion models of Savage–Hutter type for avalanches, Acta Mechanica, 199, 181–208, https://doi.org/10.1007/s00707-007-0534-9, 2008.

Chen, Y.: Research Data: Runout Mechanism of Landslides in Alluvial Basins, https://doi.org/10.57760/sciencedb.28790, 2025.

Collins, B. D. and Reid, M. E.: Enhanced landslide mobility by basal liquefaction: The 2014 State Route 530 (Oso), Washington, landslide, GSA Bulletin, 132, 451–476, https://doi.org/10.1130/B35146.1, 2019.

Community: Anura3D MPM Research Community. Anura3D Scientific Manual version 2022, 2022.

Crosta, G. B., Imposimato, S., and Roddeman, D.: Granular flows on erodible and non erodible inclines, Granular Matter, 17, 667–685, https://doi.org/10.1007/s10035-015-0587-8, 2015.

Cruden, D. M. and Hungr, O.: The debris of the Frank Slide and theories of rockslide–avalanche mobility, Canadian Journal of Earth Sciences, 23, 425–432, https://doi.org/10.1139/e86-044, 1986.

Dai, Z., Wang, F., Cheng, Q., Wang, Y., Yang, H., Lin, Q., Yan, K., Liu, F., and Li, K.: A giant historical landslide on the eastern margin of the Tibetan Plateau, Bulletin of Engineering Geology and the Environment, 78, 2055–2068, https://doi.org/10.1007/s10064-017-1226-x, 2019.

Evans, S. G., Guthrie, R. H., Roberts, N. J., and Bishop, N. F.: The disastrous 17 February 2006 rockslide-debris avalanche on Leyte Island, Philippines: a catastrophic landslide in tropical mountain terrain, Natural Hazards and Earth System Sciences, 7, 89–101, https://doi.org/10.5194/nhess-7-89-2007, 2007.

Goren, L. and Aharonov, E.: Long runout landslides: The role of frictional heating and hydraulic diffusivity, Geophysical Research Letters, 34, https://doi.org/10.1029/2006GL028895, 2007.

Guo, C., Zhang, Y., Montgomery, D. R., Du, Y., Zhang, G., and Wang, S.: How unusual is the long-runout of the earthquake-triggered giant Luanshibao landslide, Tibetan Plateau, China?, Geomorphology, 259, 145–154, https://doi.org/10.1016/j.geomorph.2016.02.013, 2016.

Guo, C., Zhang, Y., Zhang, Y., Wu, Z., Li, X., Wu, R., Yan, Y., Qiu, Z., Ren, S., and Zhao, W.: Freeze-thaw cycle effects on granite and the formation mechanism of long-runout landslides: insights from the Luanshibao case study in the Tibetan Plateau, China, Bulletin of Engineering Geology and the Environment, 82, 394, https://doi.org/10.1007/s10064-023-03427-6, 2023.

Hungr, O.: Runout Analyses of Potential Landslides of South and Third Peaks: Turtle Mountain, Alberta, AER/AGS Special Report, p. 68, 2017.

Iverson, R., George, D., Allstadt, K., Reid, M., Collins, B., Vallance, J., Schilling, S., Godt, J., Cannon, C., Magirl, C., Baum, R., Coe, J., Schulz, W., and Bower, J.: Landslide mobility and hazards: implications of the 2014 Oso disaster, Earth and Planetary Science Letters, 412, 197–208, https://doi.org/10.1016/j.epsl.2014.12.020, 2015.

Iverson, R. M. and Ouyang, C.: Entrainment of bed material by Earth-surface mass flows: Review and reformulation of depth-integrated theory, https://doi.org/10.1002/2013RG000447.

Larsen, I. J., Montgomery, D. R., and Korup, O.: Landslide erosion controlled by hillslope material, Nature Geoscience, 3, 247–251, https://doi.org/10.1038/ngeo776, 2010.

Legros, F.: The mobility of long-runout landslides, Engineering Geology, 63, 301–331, https://doi.org/10.1016/S0013-7952(01)00090-4, 2002.

Liu, W., He, S., and Li, X.: Numerical simulation of landslide over erodible surface, Geoenvironmental Disasters, 2, 19, https://doi.org/10.1186/s40677-015-0027-4, 2015.

Mangeney, A.: Landslide boost from entrainment, Nature Geoscience, 4, 77–78, https://doi.org/10.1038/ngeo1077, 2011.

Mangeney, A., Roche, O., Hungr, O., Mangold, N., Faccanoni, G., and Lucas, A.: Erosion and mobility in granular collapse over sloping beds, Journal of Geophysical Research: Earth Surface, 115, https://doi.org/10.1029/2009JF001462, 2010.

Okura, Y., Kitahara, H., Sammori, T., and Kawanami, A.: The effects of rockfall volume on runout distance, Engineering Geology, 58, 109–124, https://doi.org/10.1016/S0013-7952(00)00049-1, 2000.

Pudasaini, S. P.: A comprehensive, unified mechanical erosion model for multi-phase mass flows, International Journal of Multiphase Flow, 191, 105 328, https://doi.org/10.1016/j.ijmultiphaseflow.2025.105328, 2025.

Pudasaini, S. P. and Fischer, J.-T.: A mechanical erosion model for two-phase mass flows, International Journal of Multiphase Flow, 132, 103 416, https://doi.org/10.1016/j.ijmultiphaseflow.2020.103416, 2020.

Pudasaini, S. P. and Krautblatter, M.: The mechanics of landslide mobility with erosion, Nature Communications, 12, 6793, https://doi.org/10.1038/s41467-021-26959-5, 2021.

Pudasaini, S. P., Mergili, M., Lin, Q., and Wang, Y.: Dynamic Simulation of Rock-Avalanche Fragmentation, Journal of Geophysical Research: Earth Surface, 129, e2024JF007 689, https://doi.org/10.1029/2024JF007689, 2024.

Reid, M.: 2014 Landslide in Washington State, https://www.usgs.gov/media/images/2014-landslide-washington-state-7, [Photograph], 2017.

Ren, J., Qi, S., Xu, Z., Kang, W., Su, Q., and Lv, Y.: Timing of the Luanshibao Giant Landslide in eastern Tibet: the evidence from paleoseismology, IOP Conference Series: Earth and Environmental Science, 861, 052 002, https://doi.org/10.1088/1755-1315/861/5/052002, 2021.

Sassa, K., Fukuoka, H., Wang, G., and Ishikawa, N.: Undrained dynamic-loading ring-shear apparatus and its application to landslide dynamics, Landslides, 1, 7–19, https://doi.org/10.1007/s10346-003-0004-y, 2004.

Sassa, K., Dang, K., He, B., Takara, K., Inoue, K., and Nagai, O.: A new high-stress undrained ring-shear apparatus and its application to the 1792 Unzen–Mayuyama megaslide in Japan, Landslides, 11, 827–842, https://doi.org/10.1007/s10346-014-0501-1, 2014.

Shi, X., Jiang, L., Jiang, H., Wang, X., and Xu, J.: Geohazards Analysis of the Litang–Batang Section of Sichuan–Tibet Railway Using SAR Interferometry, IEEE Journal of Selected Topics in Applied Earth Observations and Remote Sensing, 14, 11 998–12 006, https://doi.org/10.1109/JSTARS.2021.3129270, 2021.

Vicari, H., Tran, Q.-A., Metzsch Juel, M., and Gaume, J.: The role of dilatancy and permeability of erodible wet bed sediments in affecting erosion and runout of a granular flow: Two-phase MPM–CFD simulations, Computers and Geotechnics, 185, 107 307, https://doi.org/10.1016/j.compgeo.2025.107307, 2025.

Wang, F., Sun, P., Highland, L., and Cheng, Q.: Key factors influencing the mechanism of rapid and long runout landslides triggered by the 2008 Wenchuan earthquake, China, Geoenvironmental Disasters, 1, 1, https://doi.org/10.1186/s40677-014-0001-6, 2014.

Wang, Y., Cheng, Q., Lin, Q., Li, K., and Yang, H.: Insights into the kinematics and dynamics of the Luanshibao rock avalanche (Tibetan Plateau, China) based on its complex surface landforms, Geomorphology, 317, 170–183, https://doi.org/10.1016/j.geomorph.2018.05.025, 2018.

Wang, Y., Cui, X., Che, Y., Li, P., Jiang, Y., and Peng, X.: Identification and Analysis of Unstable Slope and Seasonal Frozen Soil Area along the Litang Section of the Sichuan–Tibet Railway, China, Remote Sensing, 15, 1317, https://doi.org/10.3390/rs15051317, 2023.

Wartman, J., Montgomery, D. R., Anderson, S. A., Keaton, J. R., Benoît, J., dela Chapelle, J., and Gilbert, R.: The 22 March 2014 Oso landslide, Washington, USA, Geomorphology, 253, 275–288, https://doi.org/10.1016/j.geomorph.2015.10.022, 2016.

Wu, Y.-B., Duan, Z., Peng, J.-B., Zhang, Q., and Pähtz, T.: Influence of slope angle on deposit morphology and propagation of laboratory landslides, Scientific Reports, 13, 9452, https://doi.org/10.1038/s41598-023-36554-x, 2023.

Yerro, A., Soga, K., and Bray, J.: Runout evaluation of Oso landslide with the material point method, Canadian Geotechnical Journal, 56, 1304–1317, https://doi.org/10.1139/cgj-2017-0630, 2019.

Zeng, Q., Yuan, G., Davies, T., Xu, B., Wei, R., Xue, X., and Zhang, L.: 10Be dating and seismic origin of Luanshibao rock avalanche in SE Tibetan Plateau and implications on Litang active fault, Landslides, 17, 1091–1104, https://doi.org/10.1007/s10346-019-01319-z, 2020.

Zhang, D., Wang, J., Qi, L., Zhang, Y., Ma, J., and Lu, G.: Initiation and movement of a rock avalanche in the Tibetan Plateau, China: insights from field observations and numerical simulations, Landslides, 19, 2569–2591, https://doi.org/10.1007/s10346-022-01917-4, 2022.

Zhao, B., Zhao, X., Zeng, L., Wang, S., and Du, Y.: The mechanisms of complex morphological features of a prehistorical landslide on the eastern margin of the Qinghai-Tibetan Plateau, Bulletin of Engineering Geology and the Environment, 80, 3423–3437, https://doi.org/10.1007/s10064-021-02114-8, 2021.

Zhao, X., Wang, Y.-s., Wang, S.-y., Zhao, B., Zeng, L., Liu, Y., and Feng, Q.-q.: Nature and timing of a prehistoric giant landslide on the eastern margin of the Tibetan Plateau, Journal of Mountain Science, 17, 1438–1451, https://doi.org/10.1007/s11629-019-5831-y, 2020.

Zhu, L., Tang, X., He, S., Yang, Z., Liang, H., Lei, X., Luo, Y., and Zhang, L.: Geomorphology and Sedimentology of the Nyixoi Chongco Rock Avalanche and Implications for Emplacement Mechanisms, https://doi.org/10.1029/2024JF007666.

Zhu, L., Cui, S., Pei, X., Zhang, X., Wang, H., He, S., and Luo, L.: Investigation of the characteristics and long-runout movement mechanisms of the Luanshibao landslide on the eastern margin of the Qinghai-Tibet Plateau, Soil Dynamics and Earthquake Engineering, 153, 107 094, https://doi.org/10.1016/j.soildyn.2021.107094, 2022.